



# Geophysical Research Letters<sup>®</sup>

## RESEARCH LETTER

10.1029/2023GL107604

### Key Points:

- We report two types of energy versus latitude (or  $L$ -shell) dispersion of relativistic electron precipitation observed at ELPIN
- Both types of dispersion signatures can be attributed to electron scattering by electromagnetic ion cyclotron (EMIC) waves
- Energy dispersion is controlled by the magnetic field radial profile in the EMIC wave source region

### Supporting Information:

Supporting Information may be found in the online version of this article.

### Correspondence to:

V. S. Grach,  
vsgrach@ipfran.ru

### Citation:

Grach, V. S., Artemyev, A. V., Demekhov, A. G., Zhang, X.-J., Bortnik, J., & Angelopoulos, V. (2024). Electron precipitation driven by EMIC waves: Two types of energy dispersion. *Geophysical Research Letters*, 51, e2023GL107604. <https://doi.org/10.1029/2023GL107604>

Received 7 DEC 2023

Accepted 1 MAR 2024

### Author Contributions:

**Conceptualization:** Anton V. Artemyev, Andrei G. Demekhov, Jacob Bortnik, Vassilis Angelopoulos  
**Data curation:** Anton V. Artemyev  
**Formal analysis:** Andrei G. Demekhov  
**Investigation:** Veronika S. Grach, Anton V. Artemyev  
**Methodology:** Anton V. Artemyev, Andrei G. Demekhov  
**Resources:** Anton V. Artemyev  
**Software:** Veronika S. Grach  
**Supervision:** Jacob Bortnik, Vassilis Angelopoulos  
**Validation:** Andrei G. Demekhov, Xiao-Jia Zhang  
**Visualization:** Veronika S. Grach

© 2024, The Authors.

This is an open access article under the terms of the [Creative Commons Attribution-NonCommercial-NoDerivs License](#), which permits use and distribution in any medium, provided the original work is properly cited, the use is non-commercial and no modifications or adaptations are made.

## Electron Precipitation Driven by EMIC Waves: Two Types of Energy Dispersion

Veronika S. Grach<sup>1</sup> , Anton V. Artemyev<sup>2</sup> , Andrei G. Demekhov<sup>1,3</sup> , Xiao-Jia Zhang<sup>2,4</sup> , Jacob Bortnik<sup>2</sup> , and Vassilis Angelopoulos<sup>2</sup> 

<sup>1</sup>A.V. Gaponov-Grekhov Institute of Applied Physics, Russian Academy of Sciences, Nizhny Novgorod, Russia,

<sup>2</sup>University of California, Los Angeles, Los Angeles, CA, USA, <sup>3</sup>Polar Geophysical Institute, Apatity, Russia, <sup>4</sup>Department of Physics, University of Texas at Dallas, Richardson, TX, USA

**Abstract** Electromagnetic ion cyclotron (EMIC) waves can very rapidly and effectively scatter relativistic electrons into the atmosphere. EMIC-driven precipitation bursts can be detected by low-altitude spacecraft, and analysis of the fine structure of such bursts may reveal unique information about the near-equatorial EMIC source region. In this study, we report, for the first time, observations of EMIC-driven electron precipitation exhibiting energy,  $E$ , dispersion as a function of latitude (and hence  $L$ -shell): two predominant categories exhibit  $dE/dL > 0$  and  $dE/dL < 0$ . We interpret precipitation with  $dE/dL < 0$  as due to the typical inward radial gradient of cold plasma density and equatorial magnetic field ( $\sim 65\%$  of the statistics). Precipitation with  $dE/dL > 0$  is interpreted as due to an outward radial gradient of the equatorial magnetic field, likely produced by energetic ions freshly injected into the ring current ( $\sim 35\%$  of the statistics). The observed energy dispersion of EMIC-driven electron precipitation was reproduced in simulations.

**Plain Language Summary** Relativistic electron precipitation from the equatorial magnetosphere deposits significant energy fluxes to the atmosphere below 50 km, and thus naturally alters the atmosphere ionization and contributes to ozone destruction in the mesosphere. This precipitation is, in good part, due to electron resonant interactions with electromagnetic ion cyclotron (EMIC) waves. Although basic theories of this interaction have been well understood, the detailed electron precipitation pattern, which depends on the background plasma and magnetic field conditions in the wave source regions, are not well studied. In this study, we demonstrate a new property of electron precipitation driven by EMIC waves—the dispersion in energy versus latitude as observed by the low-altitude ELPIN CubeSats. Such dispersion can provide information about the EMIC wave source region and, as it turns out, connect relativistic electron precipitation with one of the most powerful phenomena in the magnetosphere, substorm plasma injections.

## 1. Introduction

Energetic electron resonant interaction with electromagnetic ion cyclotron (EMIC) waves is one of the key mechanisms of radiation belt depletion (e.g., Millan & Thorne, 2007; Shprits et al., 2008). High wave amplitudes and the resultant high rates of electron scattering (e.g., Summers & Thorne, 2003) make such interaction especially effective for relativistic electron losses (e.g., Drozdov et al., 2017; Kersten et al., 2014; Ma et al., 2015). Depending on the wave intensity and coherence (wave spectral width), EMIC waves can scatter electrons into the loss-cone via diffusion (Kennel & Petschek, 1966; Thorne & Kennel, 1971) or nonlinear resonant transport (Albert & Bortnik, 2009; Grach & Demekhov, 2020; Kubota et al., 2015; Omura & Zhao, 2012). The associated precipitating electron fluxes have been previously identified at low-altitude spacecraft, such as the Polar Operational Environmental Satellites (POES), in conjunction with near-equatorial or ground-based EMIC measurements (e.g., Capannolo et al., 2018, 2019; Yahnin et al., 2016; Yahnin et al., 2017). These precipitating flux measurements at low altitude can then be used to infer EMIC wave characteristics (Y. Zhang et al., 2017). Such remote sensing is particularly important, given that many details of the EMIC source region and cold plasma properties determining efficiency of electron losses often cannot be reliably measured in situ (e.g., details such as the low-intensity wave spectrum at high frequency, details of the dispersion relation as altered by the hot plasma and ion composition, etc; see discussions in Chen et al., 2019; Bashir et al., 2022; Ross et al., 2021; Angelopoulos et al., 2023). Therefore, inferring characteristics of EMIC waves from low-altitude precipitation measurements is useful to supplement statistical investigations of EMIC waves from equatorial measurements (Allen et al., 2016; Keika et al., 2013; X.-J. Zhang et al., 2016).

**Writing – original draft:** Veronika S. Grach, Anton V. Artemyev  
**Writing – review & editing:** Andrei G. Demekhov, Xiao-Jia Zhang, Jacob Bortnik, Vassilis Angelopoulos

The low energy resolution of the POES electron instrument prevents investigations of the energy-dispersion associated with EMIC-driven electron precipitation. However, a new data set of EMIC-driven precipitation events with high energy and pitch-angle resolution has been recently made available from the ELFIN CubeSat measurements (see Angelopoulos et al., 2023; Capannolo et al., 2023). This data set enables us to probe the characteristics of EMIC waves. It has been demonstrated by several case-studies of conjugate EMIC wave measurements and ELFIN observations of relativistic electron precipitation that this data set is very useful to verify theoretical models of electron scattering by EMIC waves (e.g., An et al., 2022; Angelopoulos et al., 2023; Capannolo et al., 2023; Grach et al., 2022). In this paper, we combine the theoretical model of electron precipitation due to quasi-linear and nonlinear resonant interactions with EMIC waves (Grach & Demekhov, 2018; Grach et al., 2021) and ELFIN observations of two types of EMIC-driven precipitation signatures. These two types of signatures are characterized by different energy versus  $L$ -shell dispersion of precipitating electron fluxes,  $dE/dL > 0$  or  $dE/dL < 0$ , that is, when the minimum energy of efficient electron precipitation  $E$  increases or decreases with radial distance. For the first time, we demonstrate clear evidence of both dispersion signatures in the electron precipitation data, and provide a theoretical interpretation that may be used to infer the characteristics of the EMIC wave source region.

## 2. Spacecraft Observations

We analyze in detail two events from the ELFIN data set of EMIC-driven electron precipitation (Angelopoulos et al., 2023; Capannolo et al., 2023). ELFIN CubeSats measure electrons in the energy range of 50–6000 keV with 16 energy channels and typically 8 pitch-angle channels nominally spanning the entire 0–180° range twice per  $\sim 3$  s, the spin period (Angelopoulos et al., 2023). We use three derived data products from ELFIN's electron distributions: energy spectrograms of precipitating fluxes (inside the local loss-cone,  $j_{\text{prec}}$ ), locally trapped fluxes (outside the local loss-cone,  $j_{\text{trap}}$ ), and precipitating-to-trapped flux ratios ( $j_{\text{prec}}/j_{\text{trap}}$ ). EMIC-driven precipitation events can be well distinguished by  $j_{\text{prec}}/j_{\text{trap}}$  maximizing (as a function of energy) at relativistic energies ( $j_{\text{prec}}/j_{\text{trap}} \sim 1$  above 0.5 MeV) and staying almost zero at  $\sim 100$  keV, well below the EMIC minimum resonance energy (see detailed investigations of ELFIN observed EMIC-driven precipitation in, e.g., An et al., 2022; Grach et al., 2022; Angelopoulos et al., 2023; Capannolo et al., 2023). The Supporting Information S1 shows the overview of all 84 EMIC-driven precipitation events with a clear  $dE/dL$  dispersion.

Figure 1 shows two examples of EMIC-driven precipitation events with a clear  $dE/dL$  dispersion, where  $E$  is the minimum energy for significant (i.e.,  $>0.1$ ) precipitating-to-trapped flux ratio. Panels (a1,a2) and (b1,b2) show locally trapped fluxes and precipitating-to-trapped flux ratios. ELFIN traversed from right-to-left (backwards in time) three magnetospheric regions: the plasma sheet (PS) region characterized by isotropic ( $j_{\text{prec}}/j_{\text{trap}} \sim 1$ ) fluxes of  $<200$  keV electrons (Artemyev et al., 2022); the outer radiation belt (ORB) region characterized by an energetic electron flux increase with decreasing  $L$ -shell and strongly anisotropic fluxes ( $j_{\text{prec}}/j_{\text{trap}} \ll 1$ ) including a burst of relativistic ( $>300$  keV) electron precipitation demarcated by the two vertical dashed lines; and the plasmasphere (PSh) characterized by decreased relativistic electron fluxes (which become more anisotropic due to the scattering by whistler-mode hiss waves on the dawn flank, see Mourenas et al., 2021). We will focus on the two relativistic electron bursts observed at  $\sim 23:51$  UT (in the first event) and  $\sim 11:08:40$  UT (in the second event). These bursts are due to electron scattering by EMIC waves (the absence of strong precipitation at 50–100 keV shows that this precipitation is not associated with whistler-mode waves, see discussions in Angelopoulos et al., 2023). Supporting Information S1 shows projections of ELFIN orbits relative to the Lovozero (LOZ) and Tuloma (TUL) ground-based stations during these two events (data acquisition system is described in Pil'gaev et al., 2021), which demonstrates Pc1 magnetic pulsations in conjunction with the ELFIN precipitation measurements (see panels (d1, d2)). Note, although the stations are separated from ELFIN precipitating events in latitude (but still within the range of most prolonged EMIC events, see Engebretson et al., 2015), their longitudes (corresponding to the radial scale of the projected EMIC wave source region in the equator) are quite close (Pc1 pulsations on the ground corresponding to EMIC waves in the magnetosphere are typically observed  $<1,000$  km away from their secondary source region in the ionosphere, but can still be seen as far as  $\sim 6,000$  km away, see Manchester, 1966; Manchester, 1968; Yahni et al., 2008; Liu et al., 2023). Panels (c1, c2) show the fine structure of precipitating-to-trapped flux ratio: there is a clear  $dE/dL < 0$  dispersion for the first event and  $dE/dL > 0$  dispersion for the second event. Note that the second event is longer but more structured than the first. However it appears to be composed of three separate short bursts, each burst exhibiting an increase in minimum energy of significant precipitation at progressively higher  $L$ -shells. These are quite typical dispersion signatures in our

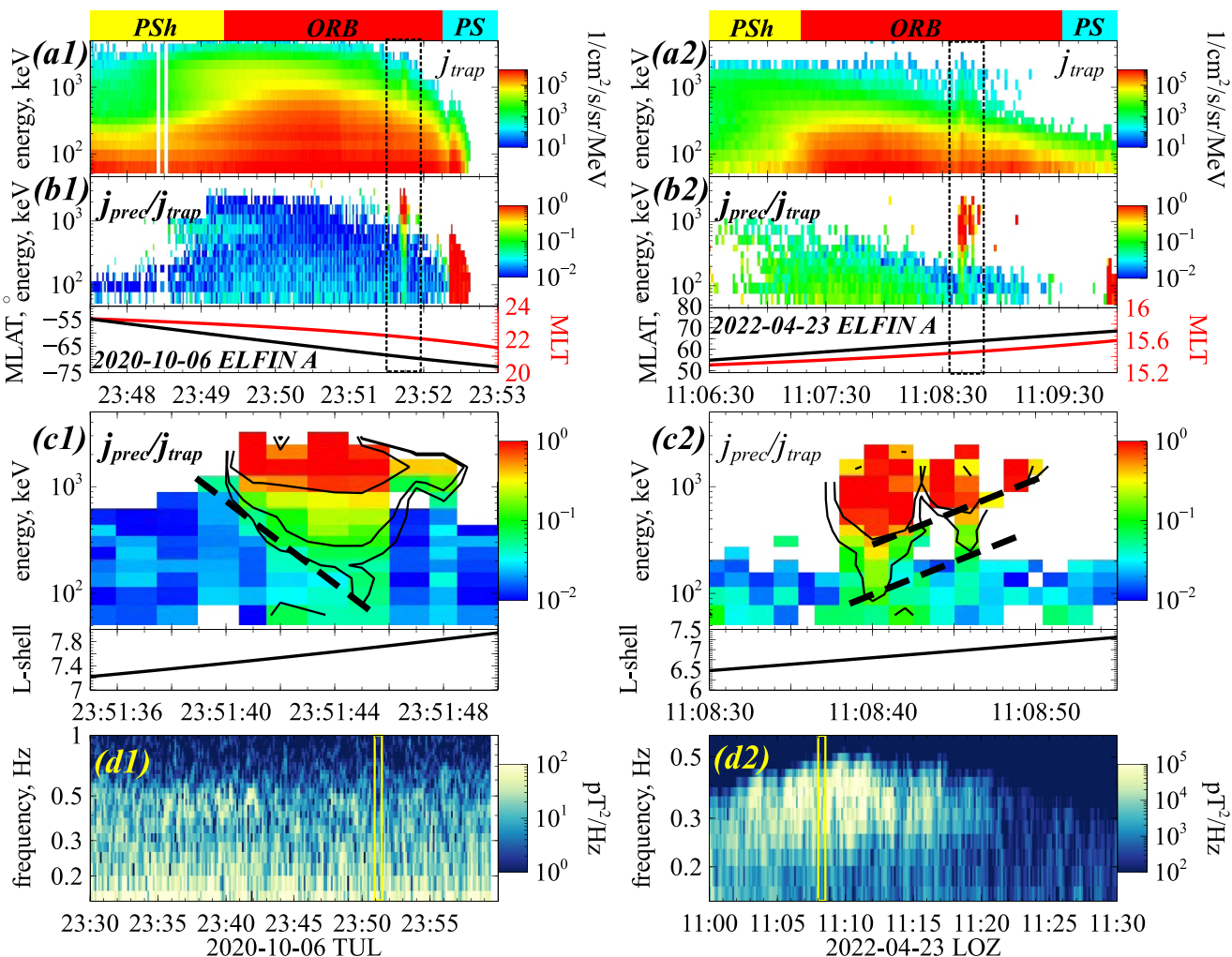


**Figure 1.** Overview of two events showing ELFIN observations of EMIC-driven precipitation in conjunction with ground-based EMIC wave observations. Panels (a1, a2) show locally trapped electron fluxes in different magnetospheric regions (as marked by the colored bars above, see details in the text). Panels (b1, b2) show precipitating-to-trapped flux ratios and ELFIN MLAT, MLT along the track. EMIC-driven precipitation bursts are shown by dashed boxes. Panels (c1, c2) show expanded views of the precipitation bursts and  $L$ -shell along ELFIN orbit (projected using the Tsyganenko, 1989, magnetic field empirical model). Panels (d1, d2) show wave spectra from the ground-based magnetometer station at LOZ, in conjunction with ELFIN at those times (see Figures S1 and S2 in Supporting Information S1 for details). The yellow vertical lines mark the intervals as in panels (c1, c2).

ELFIN data set of EMIC-driven precipitation (see Figures S2–S17 in Supporting Information S1 for 55 examples of  $dE/dL < 0$  and 29 examples of  $dE/dL > 0$  events). We now discuss the possible formation mechanisms of such dispersion.

EMIC waves are generated by a hot, transversely anisotropic ion population, which is either injected from the plasmashell and drifts duskward or heated locally at the dayside due to magnetospheric compression by solar wind transients (Jun et al., 2019, 2021; Yahnin et al., 2019). Locally enhanced plasma density (or plasma frequency to electron gyrofrequency ratio,  $f_{pe}/f_{ce}$ ), for example, within plasmaspheric plumes, can significantly intensify EMIC wave generation by decreasing the resonance energy of ions and thus increasing resonant ion fluxes (Chen et al., 2010, 2011). Such a combination of duskward ion drift and increase of  $f_{pe}/f_{ce}$  leads to EMIC wave generation and subsequent relativistic electron precipitation predominantly around the dusk-side plasmapause (Capannolo et al., 2022; Thorne & Kennel, 1971; Yahnin et al., 2016, 2017). Alternatively, EMIC waves may be generated right within the plasma sheet injection region, on the night-side (H. Kim et al., 2021), where large  $f_{pe}/f_{ce}$  is provided by the magnetic field depletion due to the diamagnetic effects of hot ions. The most representative examples of such magnetic field depletions are the so-called magnetic dips, a spatially localized magnetic field depletion filled by hot

injected ions (Xia et al., 2019; Zhu et al., 2021). Hot ions trapped within magnetic dips can generate EMIC waves (He et al., 2017; Yin et al., 2022; Yu et al., 2023). Such magnetic field depletions can change the radial gradient of the  $f_{pe}/f_{ce}$  ratio: for the dipole magnetic field  $f_{ce} \propto L^{-3}$  and empirical plasma density model (Sheeley et al., 2001)  $f_{pe} \propto L^{-2}$ , the ratio  $f_{pe}/f_{ce} \propto L$  increases with radial distance. However, for a significantly depleted magnetic field  $f_{ce} \propto L^{-3+q}$ , this ratio  $f_{pe}/f_{ce} \propto L^{1-q}$  may decrease with the radial distance (for  $q \geq 1$ ; note that around magnetic holes,  $q$  can be as large as 3 with almost no radial gradient of the magnetic field; see Zhu et al. (2021); Yin et al. (2021); Zhao et al. (2023)).

With the cold plasma approximation (note, this approximation can be violated during cases with a large population of hot ions, see, e.g. Chen et al., 2011), the minimum resonant energy of electrons scattered by EMIC waves decreases with increasing  $f/f_{ci}$  (Summers & Thorne, 2003; Ukhorskiy et al., 2010), decreases with increasing  $f_{pe}/f_{ce}$  (Summers & Thorne, 2003), and also varies with ion composition (Ross et al., 2022):

$$\frac{E_{\min}}{m_e c^2} + 1 \approx \sqrt{1 + \left(\frac{f_{ce}}{f_{pe}}\right)^2 \left(\frac{2\pi f_{pe}}{ck}\right)^2} \approx \sqrt{\frac{m_p}{m_e}} \left(\frac{f_{ce}}{f_{pe}}\right) \sqrt{\frac{f_{ci}}{f} \left(\frac{f_{ci}}{f} - 1\right)},$$

where  $k$  is the wavenumber. The factor  $f_{ci}/f$  can be either a constant (for large wave source regions where the wave frequency traces local  $f_{ci}$ ) or can vary as  $f_{ci}/f \propto L^{q-3}$  (for a localized wave source with  $f = \text{const}$  and subsequent wave spread across a large  $L$ -shell domain). In the first case, we have  $dE_{\min}/dL \propto q - 1$ , whereas in the second case and low  $f$  (such that  $f_{ci}/f - 1 \approx f_{ci}/f$ ) we have

$$\frac{1}{E_{\min}} \frac{dE_{\min}}{dL} \propto q - 1 + (q - 3) \frac{f_{ci} - \frac{1}{2}f}{f_{ci} - f} \propto 2q - 4.$$

Note the second case with  $f_{ci}/f - 1 \approx 1$  gives  $dE_{\min}/dL \propto q - 1 + (3/2)(q - 3) = (5q - 11)/2$ . For electron precipitation due to EMIC waves from a region with  $q < 2$ , we would expect a nominal dispersion  $dE/dL < 0$  (this criterion is  $q < 11/5$  for  $f_{ci}/f - 1 \approx 1$ ). However, when the waves are within a region of strongly perturbed magnetic field, where  $q > 2$ , the dispersion will be inverse,  $dE/dL > 0$ .

To verify the magnetic field deformation within the EMIC wave generation region for the event with  $dE/dL > 0$  dispersion, we examine measurements from equatorial GOES-17 (Loto'ani et al., 2019; Dichter et al., 2015; Boudouridis et al., 2020) and GEO-KOMPSAT-2A (Constantinescu et al., 2020; Magnes et al., 2020; Seon et al., 2020) spacecraft. Figure 2 shows that 1 hour before ELFIN observations of EMIC-driven precipitation at MLT  $\sim 15.6$ , there was a strong injection (around 10:10 UT) exhibiting a significant increase of energetic electron and ion fluxes. This injection is associated with a magnetic field depletion observed by GOES-17 (at MLT  $\sim 1$ ) and KOMPSAT-2A (at MLT  $\sim 18.6$ ). Observed by two near-equatorial spacecraft with a separation of  $\Delta\text{MLT} \sim 6$ , this depletion appears to be large scale. Such large regions of EMIC wave generation can exist at times of storms for  $\sim 12$  hr (see Blum et al., 2020; Engebretson et al., 2015). Although the event discussed here did not occur during a storm, it occurred under prolonged enhanced geomagnetic activity (AE peaked at  $\sim 1000$  nT at 10:30 UT and remained at or above 600 nT for an hour following that). Thus, it is reasonable to expect that the ion injection activity and associated magnetic depletions may survive until the time of ELFIN's observations of electron precipitation at 11:08 UT. Within the magnetic field depletion, KOMPSAT-2A detected helium band EMIC waves with frequencies  $\in [0.1, 0.3]$  Hz. Ground-based observations associated with ELFIN observations of precipitation show EMIC waves at higher frequencies, and thus EMIC waves responsible for the realistic electron precipitation may be generated earthward of KOMPSAT-2A (note that ELFIN's  $L$ -shell should be interpreted as only a rough estimate because of large uncertainties in mapping ELFIN to the equator, especially during enhanced substorm activity at that sector). Near its magnetic depletion region, GOES-17 also detected wave activities spanning the EMIC frequency range, but these fluctuations were broad-banded and are more likely kinetic Alfvén waves (e.g., Chaston et al., 2015) obscuring the narrow-banded, but less intense EMIC waves. In summary, Figure 2 confirms that the  $dE/dL$  dispersive event of electron precipitation observed by ELFIN is preceded by a strong plasma injection, magnetic field depletion and associated EMIC waves at geostationary orbit, in a wide MLT range near the premidnight and dusk flank sectors.

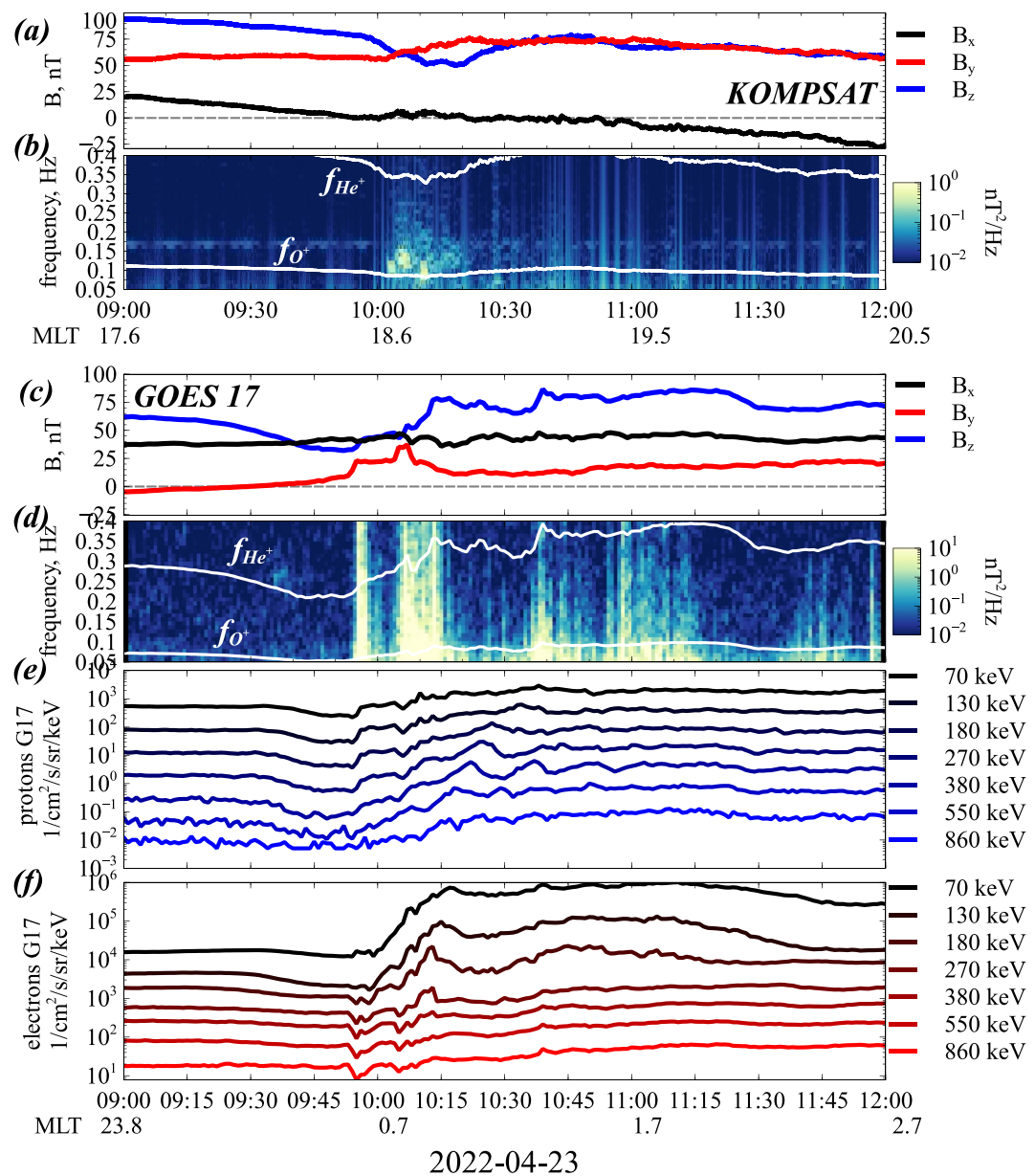


**Figure 2.** Overview of near-equatorial observations from GEO-KOMPSAT-2A and GOES-17 during the second event from Figure 1: GSM magnetic field components and magnetic field spectrum from GEO-KOMPSAT-2A (a, b), GSM magnetic field components and magnetic field spectrum from GOES-17 (c, d), ion and electron energy spectra from GOES-17 (e, f).

### 3. Simulation Setup and Results

To reproduce the energy versus  $L$ -shell dispersion in the relativistic electron precipitation signature, we perform test particle simulations with a wave packet. The wave packet is assumed to be generated by a single source near the equator and propagates along the geomagnetic field  $\mathbf{B}_0$  with wave number  $k$  and frequency  $\omega = 2\pi f$ , and amplitude  $B_w > 0$ . The packet has a finite size along the magnetic field and a much larger size across the field. The equations, describing the interaction of a relativistic electron with a given EMIC wave packet for a fixed  $L$ , follow (Grach & Demekhov, 2023; Grach et al., 2021) and are shown in Supporting Information S1. During the interaction, electron energy  $E$  approximately remains constant and the result of the interaction can be fully described by variations of the equatorial pitch-angle  $\alpha_{eq}$ .

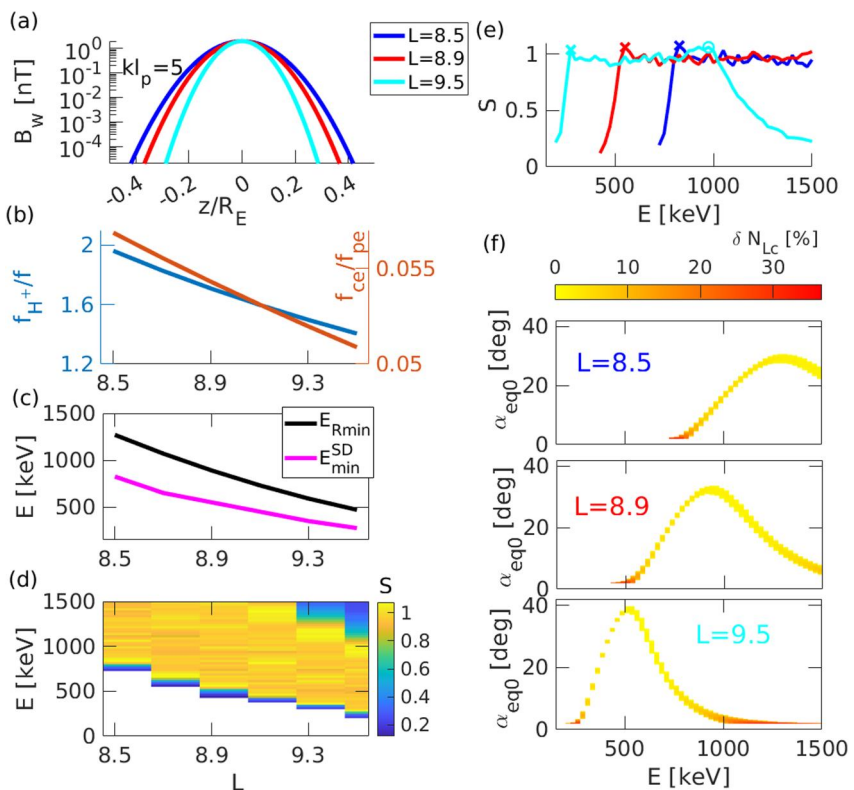


**Figure 3.** Simulation model setup and results for the first event on 06 October 2020. (a): Wave packet amplitude profile for three  $L$  values. (b): Frequency ratios as a function of  $L$ . (c): Minimum resonance energy  $E_{Rmin}$  and energy  $E_{min}^{SD}$ , corresponding to the first precipitation flux maximum (as marked by the x symbol in panel (e)). (d–e): Precipitation energy spectra as a function of  $L$ . (f): The fraction of electrons scattered into the loss cone at three  $L$  values as a function of particle initial energy and pitch-angle.

For the two events from Figure 1, simulations were run for an ensemble of test particles with various initial  $E$  and  $\alpha_{eq}$ . The parameters of plasma and wave packet are either directly based on observational data or, if such observational information is not available, are chosen from the realm of possibility to ensure a realistic simulation of the precipitation.

### 3.1. First Event, 06 October 2020

We define the wave packet frequency based on TUL data (see Figure 1d1) as  $f = \text{const} = 0.4$  Hz, which, for a dipole geomagnetic field and  $L \geq 7$ , corresponds to the hydrogen band. Taking into account ELF data (Figure 1b1), we choose  $L = 8.5\text{--}9.5$  (note that the dipole magnetic field model is likely unrealistic for such high  $L$ -shells, especially in the pre-midnight sector, hence more realistic field configurations, e.g., Sitnov et al., 2019, should be incorporated in future simulations). We assume a dipole geomagnetic field  $B_0 = B_{\text{dipole}}$ ,  $B_{\text{dipole}} \propto L^{-3}$  and gyrotropic model of the electron density  $N = N_{eq} B_0 / B_{0eq}$  with  $N_{eq} = 100 \cdot (L_{plp}/L)^4 \text{ cm}^{-3}$ , where  $L_{plp} = 4.5$  is the plasmapause location (we use the 2D plasmapause model from Pierrard & Stegen, 2008, which is available through the Community Coordinated Modeling Center), and  $N_{H^+} = N$  (note that the absence of helium ions is needed to explain the EMIC wave propagation to the ground stations, see Figure 1). The wave packet amplitude profile is chosen as  $B_w = B_{\text{max}} \exp[-z^2/(2l_p^2)]$  with  $B_{\text{max}} = 2$  nT,  $kl_p = 5$ , and is shown in Figure 3a for three values of  $L$ . The ratios  $f_{ci}/f$  ( $f_{ci} = f_{H^+}$ ) and  $f_{ce}/f_{pe}$  are shown in Figure 3b, and the corresponding minimum resonance energy  $E_{Rmin}(L)$  is shown in Figure 3c. Test particle energies are  $E = 200\text{--}1500$  keV with a 25-keV step, at initial equatorial pitch angles  $\alpha_{eq0} = \alpha_{eqLC} + 0.25^\circ\text{--}60^\circ$  (step  $0.25^\circ$ ), where  $\alpha_{eqLC} \approx 1.4^\circ\text{--}1.7^\circ$  corresponds to the loss cone at a given  $L$ .

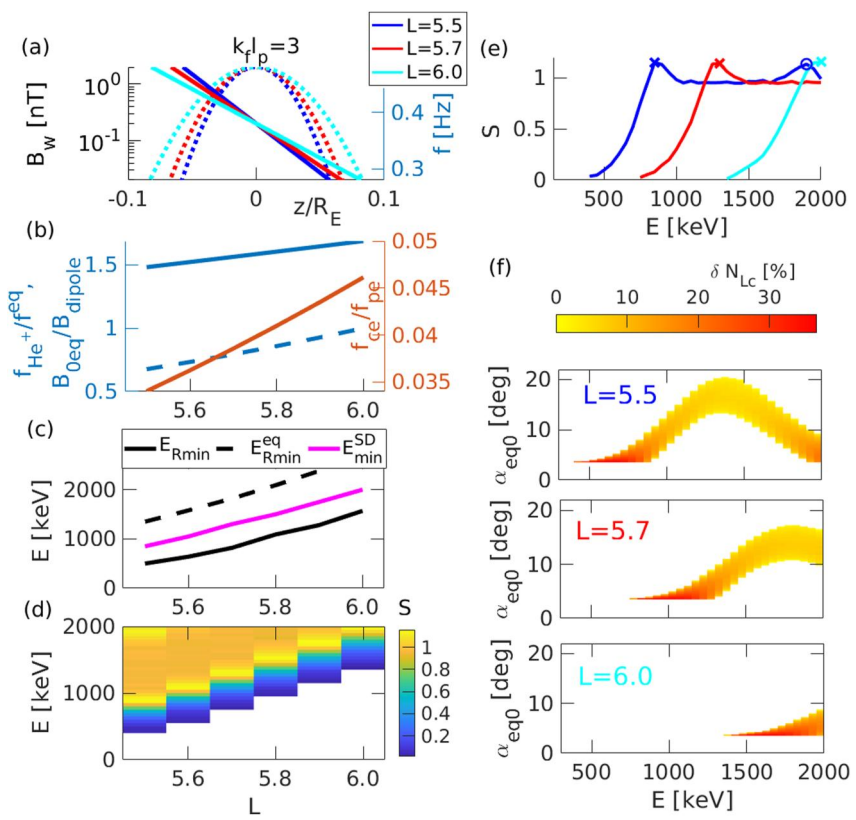


**Figure 4.** Simulation model setup and results for the second event on 23 April 2022. (a): Wave packet amplitude (dotted lines) and wave frequency (solid lines) profiles for three  $L$  values. (b): Frequency ratios (solid lines) and disturbed geomagnetic field (dashed line) as a function of  $L$ . (c): Minimum resonance energies  $E_{Rmin}$ ,  $E_{Rmin}^{eq}$  and energy  $E_{min}^{SD}$ , corresponding to the first precipitation flux maximum (as marked by the  $x$  in panel (e)). (d–e): Precipitation energy spectra as a function of  $L$ . (f): The fraction of electrons scattered into the loss cone at three  $L$  values as a function of particle initial energy and pitch-angle.

### 3.2. Second Event, 23 April 2022

Based on LOZ data, we implement a rising tone wave packet (see discussions on the rising tone formation in, e.g., Nakamura et al., 2016; Nakamura et al., 2019) with a linear frequency drift,  $f = -(f_t - f_f)z/2z_{edge} + (f_t + f_f)/2$ ,  $z_{edge} = z_f = -z_t > 0$ ,  $f_f = 0.28$  Hz,  $f_t = 0.48$  Hz (the subscripts  $f$  and  $t$  correspond to front and tail edges of the wave packet, respectively). The wave packet amplitude profile is  $B_w = B_{max} \exp[-z^2/(2l_p^2)]$  with  $B_{max} = 2$  nT,  $k_f l_p = 3$ ,  $B_w(z_f) = B_w(z_t) = 10^{-3} B_{max}$ . Such frequencies correspond to the helium band for  $L < 7$ . For  $L = 5.5$ –6.0, we introduce a perturbation of the dipole geomagnetic field as  $B_0 = (L/L_{max})^q B_{dipole}$ , where  $q = 4.5$ ,  $L_{max} = 6$  (the maximum decrease is at  $L = 5.5$ ,  $B_0 \approx 2B_{dipole}/3$ ). Electron density is  $N = N_{eq}B_0/B_{0eq}$  with  $N_{eq} = 200(L_{plp}/L)^4$  cm $^{-3}$ ,  $L_{plp} = 5$  (the same plasmapause model as above) and  $N_{H^+} = 0.8N$ ,  $N_{He^+} = 0.2N$ . Amplitude and frequency profiles for 3 values of  $L$  are shown in Figure 4a, the ratios  $B_0/B_{dipole}$ ,  $f_c/f_{eq}$  ( $f_{eq} = f|_{z=0} = (f_f + f_t)/2$ ,  $f_i = f_{He^+}$ ) and  $f_{ce}/f_{pe}$  are shown in Figure 4b. Figure 4c shows the minimum resonant energy  $E_{Rmin}$  (corresponding to the maximum wave packet frequency  $f_f$ ) and minimum resonant energy  $E_{Rmin}^{eq} > E_{Rmin}$ , corresponding to  $f_{eq}$  (with maximum amplitude). Test particle energies are  $E = 300$ –2000 keV with a 50-keV step, and  $\alpha_{eq0} = \alpha_{eqLC} + 0.25^\circ$ – $60^\circ$  (step 0.25 $^\circ$ ),  $\alpha_{eqLC} \approx 2.85^\circ$ – $3.25^\circ$ .

For both events, at each  $E$  and  $\alpha_{eq0}$ , we use 180 different initial phases  $\Psi$  that are uniformly distributed over  $[0, 2\pi]$ .

### 3.3. Simulation Results

We analyze the change in the particle equatorial pitch-angle after a single pass through the wave packet and calculate the flux ratio  $S = j_{prec}/j_{trap}$  of precipitating ( $0 \leq \alpha_{eq} < \alpha_{eqLC}$ ) and trapped ( $\alpha_{eqLC} \leq \alpha_{eq} \leq \alpha_{eqLC} + 5^\circ$ )

electrons (see Grach et al. (2022); Grach and Demekhov (2020) for the calculation details). The value  $S = 1$  corresponds to the strong diffusion limit (Kennel, 1969). In panels (b) of Figures 3 and 4, we plot  $S(E)$  for 3 values of  $L$ ; for the same  $L$  in panels (f), we plot the fraction of electrons that are scattered into the loss cone. The 2D-function  $S(E, L)$  is plotted in Figures 3d and 4d. For a fixed  $L$ , in both events  $S$  grows rapidly with energy and reaches value  $S \gtrsim 1$  at  $E = E_{\min}^{\text{SD}}$  ( $E_{\min}^{\text{SD}}$  is defined as the energy of the first precipitation flux maximum, as marked by the **x** symbol in panels (e)), stays roughly constant in the range  $E = E_{\min}^{\text{SD}} - E_{\max}^{\text{SD}}$  ( $E_{\max}^{\text{SD}}$  is defined as the energy of the last precipitation flux maximum, as marked by the **o** symbol in panels (e), though it is most often outside of the energy range of interest), and decreases smoothly with energy for  $E > E_{\max}^{\text{SD}}$ . Similar dependencies  $S(E)$  were obtained in Grach et al. (2022).

Figures 3e, 3f, 4e, and 4f show that force bunching (Bortnik et al., 2022; Grach & Demekhov, 2020; Grach et al., 2021, 2022; Kitahara & Katoh, 2019; Lundin & Shkliar, 1977) is effective at  $E = E_{\min}^{\text{SD}} - E_{\max}^{\text{SD}}$ : precipitation from small pitch angles near the loss cone is substituted by precipitation of electrons at higher  $\alpha_{\text{eq}0}$  (see discussions in Grach et al., 2022; Hanzelka, Li, & Ma, 2023), which are precipitated due to interactions in the linear regime, with possible contributions from nonlinear phase trapping that is less effective for shorter packets (see discussions in Grach et al., 2022).

As one can see from Figures 3 and 4, the function  $E_{\min}^{\text{SD}}(L)$  is similar to  $E_{\text{Rmin}}(L)$  and qualitatively follows  $f_{\text{ci}}/f, f_{\text{ce}}/f_{\text{pe}}$  giving  $dE/dL < 0$  for the first event and  $dE/dL > 0$  for the second event. Also, for the first event (at a constant frequency)  $E_{\min}^{\text{SD}} < E_{\text{Rmin}}$ , while for the second event (with a frequency drift)  $E_{\text{Rmin}} < E_{\min}^{\text{SD}} < E_{\text{Rmin}}^{\text{eq}}$ . The precipitation below  $E_{\text{Rmin}}$  is caused by the short packet length. For short packets, the wave number spectra become wider, which in turn broadens the resonant energy range and makes the interaction effective for  $E < E_{\text{Rmin}}$  (An et al., 2022; Grach & Demekhov, 2023). It was shown in Omura and Zhao (2012); Omura and Zhao (2013); Kubota and Omura (2017) that frequency drift with a rising tone makes precipitation due to nonlinear phase trapping more effective. At the same time, as discussed in Grach et al. (2022), for relatively short packets the frequency drift shifts precipitation to higher energies in comparison to packets with constant frequency (for the cases where constant frequency  $f$  is higher than the wave packet average frequency,  $f > (f_{\min} + f_{\max})/2$ ).

#### 4. Discussion and Conclusions

We have described, for the first time, detailed properties of the EMIC-driven electron precipitation signatures, that is, energy versus  $L$ -shell dispersion of precipitating electron fluxes. This dispersion can be positive  $dE/dL > 0$  or negative  $dE/dL < 0$ . The latter case is more widespread ( $55/84 = 65\%$  of the observed events) and can be explained by the typical radial gradients of equatorial plasma density  $\propto L^{-4}$  (Sheeley et al., 2001) and magnetic field  $B_{0\text{eq}} \propto L^{-3}$ , which give  $f_{\text{pe}}/f_{\text{ce}} \propto L$  and minimum resonance energy  $E_{\text{Rmin}} \propto f_{\text{ce}}/f_{\text{pe}} \propto L^{-1}$  for a fixed  $f/f_{\text{ci}}$  and a spatially broad EMIC source. A more realistic, spatially localized EMIC source (Blum et al., 2016, 2017) with fixed  $f$  and wave spreading during propagation (e.g., E.-H. Kim & Johnson, 2016; Hanzelka, Li, Ma, Qin, et al., 2023) will lead to a stronger  $E$  dependence on  $L$  and make the  $dE/dL < 0$  dispersion more evident. The positive dispersion of electron precipitation,  $dE/dL > 0$ , observed for  $29/84 = 35\%$  of events, requires a significant deformation of the equatorial magnetic field configuration,  $B_{0\text{eq}} \propto L^{-3+q}$ . For a spatially distributed wave source with fixed  $f/f_{\text{ci}}$ , we have  $E \propto f_{\text{ce}}/f_{\text{pe}} \propto L^{q-1}$ , and  $q > 1$  is required. A more realistic, spatially localized EMIC source (Blum et al., 2016, 2017) with fixed  $f$  would require  $q > 2$  to reverse  $E \propto (f_{\text{ce}}/f_{\text{pe}})(f_{\text{ci}}/f) \propto L^{2q-4}$  variation with  $L$  and lead to  $dE/dL > 0$ . Both dispersions have been reproduced in the test particle simulation model with the observed EMIC wave characteristics.

The observations and simulation results suggest that low-altitude measurements of electron precipitation, if well resolved in time and energy, may reveal not only wave characteristics (as has been shown in Y. Zhang et al., 2017; Li et al., 2013; Shumko et al., 2021), but also characteristics of the equatorial wave generation region. For example, the magnetic field deformation required to explain the positive dispersion,  $dE/dL > 0$ , is likely produced by diamagnetic currents of hot injected ions (Yin et al., 2021; Zhao et al., 2023; Zhu et al., 2021). Therefore, the difference between  $dE/dL > 0$  and  $dE/dL < 0$  events may be attributed to the difference of the equatorial ion pressure within the EMIC wave generation region (see details in Xia et al., 2019; Zhu et al., 2021).

Although in this study we propose the magnetic field depletion by hot injected ions as a viable candidate for the formation of  $dE/dL > 0$  dispersion, there are other possible alternatives due to plasma density gradients instead of magnetic field gradients. As shown in Supporting Information S1,  $\sim 50\%$  events with  $dE/dL > 0$  are observed at

the dusk flank, where plasma density plumes are often detected (e.g., Darrouzet et al., 2008). Such plumes can produce EMIC waves (Chen et al., 2009), guide them to higher latitudes (Hanzelka, Li, Ma, Qin, et al., 2023), and decrease the electron minimum resonant energy due to high density (high  $f_{pe}/f_{ce}$ ). Generation of  $dE/dL > 0$  dispersion within plasma plumes may be explained by the strong density ( $f_{pe}/f_{ce}$ ) gradient and requires further investigation via numerical simulations.

## Data Availability Statement

Fluxes measured by ELFIN are available in ELFIN data archive (ELFIN, 2024) in CDF format. Ground-based measurements of wave magnetic field at LOZ and TUL stations are available at (PGIA, 2024). GOES-R magnetic field and energetic particle fluxes are available at (GOES-R, 2024). GEO-KOMPSAT-2A (SOSMAG) data is made available (following registration) via ESA's Space Safety Programme and its provision forms part of the ESA Space Weather Service System at (SOSMAG, 2024). In this study we use Recalibrated L2 Magnetic Field Data set, SOSMAG-GK-2A-L2. Data analysis was done using SPEDAS V4.1 (Angelopoulos et al., 2019).

## Acknowledgments

We acknowledge one of the reviewers for useful discussions on the possible role of plasma plumes in the formation of  $dE/dL > 0$  dispersive precipitation. We are grateful to NASA's CubeSat Launch Initiative for ELFIN's successful launch in the desired orbits. We acknowledge early support of ELFIN project by the AFOSR, under its University Nanosat Program, UNP-8 project, contract FA9453-12-D-0285, and by the California Space Grant program. We acknowledge critical contributions of numerous volunteer ELFIN team student members. We acknowledge Niklas Grimmich for important help with GEO-KOMPSAT-2A magnetic field data, and GEO-KOMPSAT-2A magnetometer team for excellent quality data set; Ulrich Auster, Dragos Constantinescu, Ferdinand Plaschke (Institut für Geophysik und Extraterrestrische Physik, Technische Universität Braunschweig, Braunschweig, Germany) and Delva Magda, Magnes Werner, and David Fischer (Space Research Institute, Austrian Academy of Science, Graz, Austria). We appreciate the access to LOZ and TUL Pe1 data (PI: Yury Fedorenko). V.S.G. acknowledges support from RSF Grant 19-72-10111 (numerical simulations in Section 3). A.V.A., X.-J.Z., and J.B. acknowledge support from the NASA Grant 80NSSC20K1270. X.-J.Z. acknowledges support from the NSF Grant 2329897 and NASA Grants 80NSSC23K0403, 80NSSC20K0689. A.G.D. acknowledges support from the Russian science foundation Grant 22-62-00048. V.A. acknowledge support by NSF Grants AGS-1242918, AGS-2019950.

## References

Albert, J. M., & Bortnik, J. (2009). Nonlinear interaction of radiation belt electrons with electromagnetic ion cyclotron waves. *Geophysical Research Letters*, 36(12), 12110. <https://doi.org/10.1029/2009GL038904>

Allen, R. C., Zhang, J. C., Kistler, L. M., Spence, H. E., Lin, R. L., Klecker, B., et al. (2016). A statistical study of EMIC waves observed by Cluster: 2. Associated plasma conditions. *Journal of Geophysical Research: Space Physics*, 121(7), 6458–6479. <https://doi.org/10.1002/2016JA022541>

An, X., Artemyev, A., Angelopoulos, V., Zhang, X., Mourenas, D., & Bortnik, J. (2022). Nonresonant scattering of relativistic electrons by electromagnetic ion cyclotron waves in Earth's radiation belts. *Physical Review Letters*, 129(13), 135101. <https://doi.org/10.1103/PhysRevLett.129.135101>

Angelopoulos, V., Cruce, P., Drozdov, A., Grimes, E. W., Hatzigeorgiu, N., King, D. A., et al. (2019). The Space Physics Environment Data Analysis System (SPEDAS). *Space Science Reviews*, 215(1), 9. <https://doi.org/10.1007/s11214-018-0576-4>

Angelopoulos, V., Zhang, X. J., Artemyev, A. V., Mourenas, D., Tsai, E., Wilkins, C., et al. (2023). Energetic electron precipitation driven by electromagnetic ion cyclotron waves from ELFIN's low altitude perspective. *Space Science Reviews*, 219(5), 37. <https://doi.org/10.1007/s11214-023-00984-w>

Artemyev, A. V., Angelopoulos, V., Zhang, X. J., Runov, A., Petrukovich, A., Nakamura, R., et al. (2022). Thinning of the magnetotail current sheet inferred from low-altitude observations of energetic electrons. *Journal of Geophysical Research: Space Physics*, 127(10), e2022JA030705. <https://doi.org/10.1029/2022JA030705>

Bashir, M. F., Artemyev, A., Zhang, X.-J., & Angelopoulos, V. (2022). Hot plasma effects on electron resonant scattering by electromagnetic ion cyclotron waves. *Geophysical Research Letters*, 49(11), e99229. <https://doi.org/10.1029/2022GL099229>

Blum, L. W., Agapitov, O., Bonnell, J. W., Kletzing, C., & Wygant, J. (2016). EMIC wave spatial and coherence scales as determined from multipoint Van Allen Probe measurements. *Geophysical Research Letters*, 43(10), 4799–4807. <https://doi.org/10.1002/2016GL068799>

Blum, L. W., Bonnell, J. W., Agapitov, O., Paulson, K., & Kletzing, C. (2017). EMIC wave scale size in the inner magnetosphere: Observations from the dual Van Allen Probes. *Geophysical Research Letters*, 44(3), 1227–1233. <https://doi.org/10.1002/2016GL072316>

Blum, L. W., Remya, B., Denton, M. H., & Schiller, Q. (2020). Persistent EMIC wave activity across the nightside inner magnetosphere. *Geophysical Research Letters*, 47(6), e87009. <https://doi.org/10.1029/2020GL087009>

Bortnik, J., Albert, J. M., Artemyev, A., Li, W., Jun, C.-W., Grach, V. S., & Demekhov, A. G. (2022). Amplitude dependence of nonlinear precipitation blocking of relativistic electrons by large amplitude EMIC waves. *Geophysical Research Letters*, 49(12), e98365. <https://doi.org/10.1029/2022GL098365>

Boudouridis, A., Rodriguez, J. V., Kress, B. T., Dichter, B. K., & Onsager, T. G. (2020). Development of a Bowtie inversion technique for real-time processing of the GOES-16/-17 SEISS MPS-HI electron channels. *Space Weather*, 18(4), e02403. <https://doi.org/10.1029/2019SW002403>

Capannolo, L., Li, W., Ma, Q., Chen, L., Shen, X. C., Spence, H. E., et al. (2019). Direct observation of sub-relativistic electron precipitation potentially driven by EMIC waves. *Geophysical Research Letters*, 46(22), 12711–12721. <https://doi.org/10.1029/2019GL084202>

Capannolo, L., Li, W., Ma, Q., Qin, M., Shen, X. C., Angelopoulos, V., et al. (2023). Electron precipitation observed by ELFIN using proton precipitation as a proxy for electromagnetic ion cyclotron (EMIC) waves. *Geophysical Research Letters*, 50(21), e2023GL103519. <https://doi.org/10.1029/2023GL103519>

Capannolo, L., Li, W., Ma, Q., Zhang, X.-J., Redmon, R. J., Rodriguez, J. V., et al. (2018). Understanding the driver of energetic electron precipitation using coordinated multisatellite measurements. *Geophysical Research Letters*, 45(14), 6755–6765. <https://doi.org/10.1029/2018GL078604>

Capannolo, L., Li, W., Millan, R., Smith, D., Sivadas, N., Sample, J., & Shekhar, S. (2022). Relativistic electron precipitation near midnight: Drivers, distribution, and properties. *Journal of Geophysical Research: Space Physics*, 127(1), e2021JA030111. <https://doi.org/10.1029/2021JA030111>

Chaston, C. C., Bonnell, J. W., Kletzing, C. A., Hospodarsky, G. B., Wygant, J. R., & Smith, C. W. (2015). Broadband low-frequency electromagnetic waves in the inner magnetosphere. *Journal of Geophysical Research*, 120(10), 8603–8615. <https://doi.org/10.1002/2015JA021690>

Chen, L., Thorne, R. M., & Bortnik, J. (2011). The controlling effect of ion temperature on EMIC wave excitation and scattering. *Geophysical Research Letters*, 38(16), L16109. <https://doi.org/10.1029/2011GL048653>

Chen, L., Thorne, R. M., & Horne, R. B. (2009). Simulation of EMIC wave excitation in a model magnetosphere including structured high-density plumes. *Journal of Geophysical Research*, 114(A7), A07221. <https://doi.org/10.1029/2009JA014204>

Chen, L., Thorne, R. M., Jordanova, V. K., Wang, C.-P., Gkioulidou, M., Lyons, L., & Horne, R. B. (2010). Global simulation of EMIC wave excitation during the 21 April 2001 storm from coupled RCM-RAM-HOTRAY modeling. *Journal of Geophysical Research*, 115(A7), A07209. <https://doi.org/10.1029/2009JA015075>

Chen, L., Zhu, H., & Zhang, X. (2019). Wavenumber analysis of EMIC waves. *Geophysical Research Letters*, 46(11), 5689–5697. <https://doi.org/10.1029/2019GL082686>

Constantinescu, O. D., Auster, H.-U., Delva, M., Hillenmaier, O., Magnes, W., & Plaschke, F. (2020). Principal component gradiometer technique for removal of spacecraft-generated disturbances from magnetic field data. *Geoscientific Instrumentation, Methods and Data Systems Discussions*, 25, 1–26. <https://doi.org/10.5194/gi-2020-10>

Darrouzet, F., de Keyser, J., Décréau, P. M. E., El Lemdani-Mazouz, F., & Vallières, X. (2008). Statistical analysis of plasmaspheric plumes with Cluster/WHISPER observations. *Annales Geophysicae*, 26(8), 2403–2417. <https://doi.org/10.5194/angeo-26-2403-2008>

Dichter, B. K., Galica, G. E., McGarity, J. O., Tsui, S., Golightly, M. J., Lopate, C., & Connell, J. J. (2015). Specification, design, and calibration of the space weather suite of instruments on the NOAA GOES-R program spacecraft. *IEEE Transactions on Nuclear Science*, 62(6), 2776–2783. <https://doi.org/10.1109/TNS.2015.2477997>

Drozdov, A. Y., Shprits, Y. Y., Usanova, M. E., Aseev, N. A., Kellerman, A. C., & Zhu, H. (2017). EMIC wave parameterization in the long-term VERB code simulation. *Journal of Geophysical Research*, 122(8), 8488–8501. <https://doi.org/10.1002/2017JA024389>

ELFIN. (2024). Electron losses and fields investigation (ELFIN) data archive. [Dataset]. *ELFIN*. Retrieved from <https://data.elfin.ucla.edu/>

Engelbreton, M. J., Posch, J. L., Wygant, J. R., Kletzing, C. A., Lessard, M. R., Huang, C.-L., et al. (2015). Van Allen probes, NOAA, GOES, and ground observations of an intense EMIC wave event extending over 12 h in magnetic local time. *Journal of Geophysical Research*, 120(7), 5465–5488. <https://doi.org/10.1002/2015JA021227>

GOES-R. (2024). Geostationary operational environmental satellites (GOES-R) magnetic field and energetic particle fluxes data archive. [Dataset]. *GOES-R*. Retrieved from <https://www.ngdc.noaa.gov/stp/satellite/goes/>

Grach, V. S., Artemyev, A. V., Demekhov, A. G., Zhang, X.-J., Bortnik, J., Angelopoulos, V., et al. (2022). Relativistic electron precipitation by EMIC waves: Importance of nonlinear resonant effects. *Geophysical Research Letters*, 49(17), e99994. <https://doi.org/10.1029/2022GL099994>

Grach, V. S., & Demekhov, A. G. (2018). Resonant interaction of relativistic electrons with electromagnetic ion-cyclotron waves. II. Integral parameters of interaction regimes. *Radiophysics and Quantum Electronics*, 61(6), 389–401. <https://doi.org/10.1007/s11141-018-9900-9>

Grach, V. S., & Demekhov, A. G. (2020). Precipitation of relativistic electrons under resonant interaction with electromagnetic ion cyclotron wave packets. *Journal of Geophysical Research: Space Physics*, 125(2), e27358. <https://doi.org/10.1029/2019JA027358>

Grach, V. S., & Demekhov, A. G. (2023). Interaction of relativistic electrons with packets of the electromagnetic ion cyclotron waves of finite length and low amplitude. *Plasma Physics Reports*, 49(7), 901–911. <https://doi.org/10.1134/S1063780X23600561>

Grach, V. S., Demekhov, A. G., & Larchenko, A. V. (2021). Resonant interaction of relativistic electrons with realistic electromagnetic ion-cyclotron wave packets. *Earth Planets and Space*, 73(1), 129. <https://doi.org/10.1186/s40623-021-01453-w>

Hanzelka, M., Li, W., & Ma, Q. (2023). Parametric analysis of pitch angle scattering and losses of relativistic electrons by oblique EMIC waves. *Frontiers in Astronomy and Space Sciences*, 10, 1163515. <https://doi.org/10.3389/fspas.2023.1163515>

Hanzelka, M., Li, W., Ma, Q., Qin, M., Shen, X.-C., Capannolo, L., & Gan, L. (2023). Full-wave modeling of emic wave packets: Ducted propagation and reflected waves. *Frontiers in Astronomy and Space Sciences*, 10. <https://doi.org/10.3389/fspas.2023.1251563>

He, Z., Chen, L., Zhu, H., Xia, Z., Reeves, G. D., Xiong, Y., et al. (2017). Multiple-satellite observation of magnetic dip event during the substorm on 10 October 2013. *Geophysical Research Letters*, 44(18), 9167–9175. <https://doi.org/10.1002/2017GL074869>

Jun, C.-W., Miyoshi, Y., Kurita, S., Yue, C., Bortnik, J., Lyons, L., et al. (2021). The characteristics of EMIC waves in the magnetosphere based on the Van Allen Probes and arase observations. *Journal of Geophysical Research: Space Physics*, 126(6), e29001. <https://doi.org/10.1029/2020JA029001>

Jun, C. W., Yue, C., Bortnik, J., Lyons, L. R., Nishimura, Y., & Kletzing, C. (2019). EMIC wave properties associated with and without injections in the inner magnetosphere. *Journal of Geophysical Research: Space Physics*, 124(3), 2029–2045. <https://doi.org/10.1029/2018JA026279>

Keika, K., Takahashi, K., Ukhorskiy, A. Y., & Miyoshi, Y. (2013). Global characteristics of electromagnetic ion cyclotron waves: Occurrence rate and its storm dependence. *Journal of Geophysical Research*, 118(7), 4135–4150. <https://doi.org/10.1002/jgra.50385>

Kennel, C. F. (1969). Consequences of a magnetospheric plasma. *Reviews of Geophysics and Space Physics*, 7(1–2), 379–419. <https://doi.org/10.1029/RG007i001p00379>

Kennel, C. F., & Petschek, H. E. (1966). Limit on stably trapped particle fluxes. *Journal of Geophysical Research*, 71, 1–28. <https://doi.org/10.1029/jz071i001p00001>

Kersten, T., Horne, R. B., Glauert, S. A., Meredith, N. P., Fraser, B. J., & Grew, R. S. (2014). Electron losses from the radiation belts caused by EMIC waves. *Journal of Geophysical Research*, 119(11), 8820–8837. <https://doi.org/10.1002/2014JA020366>

Kim, E.-H., & Johnson, J. R. (2016). Full-wave modeling of EMIC waves near the  $\text{He}^+$  gyrofrequency. *Geophysical Research Letters*, 43(1), 13–21. <https://doi.org/10.1002/2015GL066978>

Kim, H., Schiller, Q., Engelbreton, M. J., Noh, S., Kuzichev, I., Lanzerotti, L. J., et al. (2021). Observations of particle loss due to injection associated electromagnetic ion cyclotron waves. *Journal of Geophysical Research: Space Physics*, 126(2), e28503. <https://doi.org/10.1029/2020JA028503>

Kitahara, M., & Katoh, Y. (2019). Anomalous trapping of low pitch angle electrons by coherent whistler mode waves. *Journal of Geophysical Research*, 124(7), 5568–5583. <https://doi.org/10.1029/2019JA026493>

Kubota, Y., & Omura, Y. (2017). Rapid precipitation of radiation belt electrons induced by EMIC rising tone emissions localized in longitude inside and outside the plasmapause. *Journal of Geophysical Research: Space Physics*, 122(1), 293–309. <https://doi.org/10.1002/2016JA023267>

Kubota, Y., Omura, Y., & Summers, D. (2015). Relativistic electron precipitation induced by EMIC-triggered emissions in a dipole magnetosphere. *Journal of Geophysical Research: Space Physics*, 120(6), 4384–4399. <https://doi.org/10.1002/2015JA021017>

Li, W., Ni, B., Thorne, R. M., Bortnik, J., Green, J. C., Kletzing, C. A., et al. (2013). Constructing the global distribution of chorus wave intensity using measurements of electrons by the POES satellites and waves by the Van Allen Probes. *Geophysical Research Letters*, 40(17), 4526–4532. <https://doi.org/10.1002/grl.50920>

Liu, J., Shiokawa, K., Oyama, S.-I., Otsuka, Y., Jun, C.-W., Nosé, M., et al. (2023). A statistical study of longitudinal extent of  $\text{Pc}1$  pulsations using seven PWING ground stations at subauroral latitudes. *Journal of Geophysical Research: Space Physics*, 128(1), e2021JA029987. <https://doi.org/10.1029/2021JA029987>

Loto'aniu, T. M., Redmon, R. J., Calif, S., Singer, H. J., Rowland, W., Macintyre, S., et al. (2019). The GOES-16 spacecraft science magnetometer. *Space Science Reviews*, 215(4), 32. <https://doi.org/10.1007/s11214-019-0600-3>

Lundin, B. V., & Shkliar, D. R. (1977). Interaction of electrons with low transverse velocities with VLF waves in an inhomogeneous plasma. *Geomagnetism and Aeronomy*, 17, 246–251.

Ma, Q., Li, W., Thorne, R. M., Ni, B., Kletzing, C. A., Kurth, W. S., et al. (2015). Modeling inward diffusion and slow decay of energetic electrons in the Earth's outer radiation belt. *Geophysical Research Letters*, 42(4), 987–995. <https://doi.org/10.1002/2014GL062977>

Magnes, W., Hillenmaier, O., Auster, H. U., Brown, P., Kraft, S., Seon, J., et al. (2020). Space weather magnetometer aboard GEO-KOMPSAT-2A. *Space Science Reviews*, 216(8), 119. <https://doi.org/10.1007/s11214-020-00742-2>

Manchester, R. N. (1966). Propagation of Pc 1 micropulsations from high to low latitudes. *Journal of Geophysical Research*, 71(15), 3749–3754. <https://doi.org/10.1029/JZ071i015p03749>

Manchester, R. N. (1968). Correction of Pc 1 micropulsations at spaced stations. *Journal of Geophysical Research*, 73(11), 3549–3556. <https://doi.org/10.1029/JA073i011p03549>

Millan, R. M., & Thorne, R. M. (2007). Review of radiation belt relativistic electron losses. *Journal of Atmospheric and Solar-Terrestrial Physics*, 69(3), 362–377. <https://doi.org/10.1016/j.jastp.2006.06.019>

Mourenas, D., Artemyev, A. V., Zhang, X. J., Angelopoulos, V., Tsai, E., & Wilkins, C. (2021). Electron lifetimes and diffusion rates inferred from ELFIN measurements at low altitude: First results. *Journal of Geophysical Research: Space Physics*, 126(11), e29757. <https://doi.org/10.1029/2021JA029757>

Nakamura, S., Omura, Y., & Angelopoulos, V. (2016). A statistical study of EMIC rising and falling tone emissions observed by THEMIS. *Journal of Geophysical Research: Space Physics*, 121(9), 8374–8391. <https://doi.org/10.1002/2016JA022353>

Nakamura, S., Omura, Y., Kletzing, C., & Baker, D. N. (2019). Rapid precipitation of relativistic electron by EMIC rising-tone emissions observed by the Van Allen Probes. *Journal of Geophysical Research: Space Physics*, 124(8), 6701–6714. <https://doi.org/10.1029/2019JA026772>

Omura, Y., & Zhao, Q. (2012). Nonlinear pitch angle scattering of relativistic electrons by EMIC waves in the inner magnetosphere. *Journal of Geophysical Research*, 117(A16), 8227. <https://doi.org/10.1029/2012JA017943>

Omura, Y., & Zhao, Q. (2013). Relativistic electron microbursts due to nonlinear pitch angle scattering by EMIC triggered emissions. *Journal of Geophysical Research*, 118(8), 5008–5020. <https://doi.org/10.1002/jgra.50477>

PGIA. (2024). Ground-based measurements of wave magnetic field data archive. [Dataset]. PGIA. Retrieved from <http://aurora.pgia.ru:8071/index.php?p=0&s=2&x=MELZ&t=1650672000>

Pierrard, V., & Stegen, K. (2008). A three-dimensional dynamic kinetic model of the plasmasphere. *Journal of Geophysical Research*, 113(A10), A10209. <https://doi.org/10.1029/2008JA013060>

Pil'gaev, S. V., Larchenko, A. V., Fedorenko, Y. V., Filatov, M. V., & Nikitenko, A. S. (2021). A three-component very-low-frequency signal receiver with precision data synchronization with universal time. *Instruments and Experimental Techniques*, 64(5), 744–753. <https://doi.org/10.1134/s0020441221040229>

Ross, J. P. J., Glauert, S. A., Horne, R. B., & Meredith, N. P. (2022). The importance of ion composition for radiation belt modeling. *Journal of Geophysical Research: Space Physics*, 127(9), e30680. <https://doi.org/10.1029/2022JA030680>

Ross, J. P. J., Glauert, S. A., Horne, R. B., Watt, C. E. J., & Meredith, N. P. (2021). On the variability of EMIC waves and the consequences for the relativistic electron radiation belt population. *Journal of Geophysical Research: Space Physics*, 126(12), e29754. <https://doi.org/10.1029/2021JA029754>

Seon, J., Chae, K. S., Na, G. W., Seo, H. K., Shin, Y. C., Woo, J., et al. (2020). Particle detector (PD) experiment of the Korea space environment monitor (KSEM) aboard geostationary satellite GK2A. *Space Science Reviews*, 216(1), 13. <https://doi.org/10.1007/s11214-020-0636-4>

Sheeley, B. W., Moldwin, M. B., Rassoul, H. K., & Anderson, R. R. (2001). An empirical plasmasphere and trough density model: CRRES observations. *Journal of Geophysical Research*, 106(A11), 25631–25642. <https://doi.org/10.1029/2000JA000286>

Shprits, Y. Y., Subbotin, D. A., Meredith, N. P., & Elkington, S. R. (2008). Review of modeling of losses and sources of relativistic electrons in the outer radiation belt II: Local acceleration and loss. *Journal of Atmospheric and Solar-Terrestrial Physics*, 70(14), 1694–1713. <https://doi.org/10.1016/j.jastp.2008.06.014>

Shumko, M., Blum, L. W., & Crew, A. B. (2021). Duration of individual relativistic electron microbursts: A probe into their scattering mechanism. *Geophysical Research Letters*, 48(17), e93879. <https://doi.org/10.1029/2021GL093879>

Sitnov, M. I., Birn, J., Ferdousi, B., Gordeev, E., Khotyaintsev, Y., Merkin, V., et al. (2019). Explosive magnetotail activity. *Space Science Reviews*, 215(4), 31. <https://doi.org/10.1007/s11214-019-0599-5>

SOSMAG. (2024). GEO-KOMPSAT-2A data base. [Dataset]. SOSMAG. Retrieved from <https://swe.ssa.esa.int/>

Summers, D., & Thorne, R. M. (2003). Relativistic electron pitch-angle scattering by electromagnetic ion cyclotron waves during geomagnetic storms. *Journal of Geophysical Research*, 108(A4), 1143. <https://doi.org/10.1029/2002JA009489>

Thorne, R. M., & Kennel, C. F. (1971). Relativistic electron precipitation during magnetic storm main phase. *Journal of Geophysical Research*, 76(19), 4446–4453. <https://doi.org/10.1029/JA076i019p04446>

Tsyganenko, N. A. (1989). A magnetospheric magnetic field model with a warped tail current sheet. *Planetary and Space Science*, 37(1), 5–20. [https://doi.org/10.1016/0032-0633\(89\)90066-4](https://doi.org/10.1016/0032-0633(89)90066-4)

Ukhorskiy, A. Y., Shprits, Y. Y., Anderson, B. J., Takahashi, K., & Thorne, R. M. (2010). Rapid scattering of radiation belt electrons by storm-time EMIC waves. *Geophysical Research Letters*, 37(9), L09101. <https://doi.org/10.1029/2010GL042906>

Xia, Z., Chen, L., Artemyev, A., Zhu, H., Jordanova, V. K., & Zheng, L. (2019). The effects of localized thermal pressure on equilibrium magnetic fields and particle drifts in the inner magnetosphere. *Journal of Geophysical Research: Space Physics*, 124(7), 5129–5142. <https://doi.org/10.1029/2018JA026043>

Yahnin, A. G., Titova, E. E., Demekhov, A. G., Yahnina, T. A., Popova, T. A., Lubchich, A. A., et al. (2019). Simultaneous observations of EMIC waves, ELF/VLF waves, and energetic particle precipitation during multiple compressions of the magnetosphere. *Geomagnetism and Aeronomy*, 59(6), 668–680. <https://doi.org/10.1134/S0016793219060148>

Yahnin, A. G., Yahnina, T. A., & Frey, H. U. (2008). Identification of sources of Pc1 geomagnetic pulsations on the basis of proton aurora observations. *Cosmic Research*, 46(4), 335–338. <https://doi.org/10.1134/S0010952508040084>

Yahnin, A. G., Yahnina, T. A., Raita, T., & Manninen, J. (2017). Ground pulsation magnetometer observations conjugated with relativistic electron precipitation. *Journal of Geophysical Research: Space Physics*, 122(9), 9169–9182. <https://doi.org/10.1002/2017JA024249>

Yahnin, A. G., Yahnina, T. A., Semenova, N. V., Gvozdevsky, B. B., & Pashin, A. B. (2016). Relativistic electron precipitation as seen by NOAA POES. *Journal of Geophysical Research: Space Physics*, 121(9), 8286–8299. <https://doi.org/10.1002/2016JA022765>

Yin, Z.-F., Zhou, X.-Z., Hu, Z.-J., Yue, C., Zong, Q.-G., Hao, Y.-X., et al. (2022). Localized excitation of electromagnetic ion cyclotron waves from anisotropic protons filtered by magnetic dips. *Journal of Geophysical Research: Space Physics*, 127(6), e30531. <https://doi.org/10.1029/2022JA030531>

Yin, Z.-F., Zhou, X.-Z., Zong, Q.-G., Liu, Z.-Y., Yue, C., Xiong, Y., et al. (2021). Inner magnetospheric magnetic dips and energetic protons trapped therein: Multi spacecraft observations and simulations. *Geophysical Research Letters*, 48(7), e92567. <https://doi.org/10.1029/2021GL092567>

Yu, X., Yuan, Z., Huang, Z., Xue, Z., & Zhao, Y. (2023). Effects of magnetic dips on the propagation of electromagnetic ion cyclotron waves. *Journal of Geophysical Research: Space Physics*, 128(3), e2022JA031178. <https://doi.org/10.1029/2022JA031178>

Zhang, X.-J., Li, W., Thorne, R. M., Angelopoulos, V., Bortnik, J., Kletzing, C. A., et al. (2016). Statistical distribution of EMIC wave spectra: Observations from Van Allen Probes. *Geophysical Research Letters*, 43(24), 12. <https://doi.org/10.1002/2016GL071158>

Zhang, Y., Shi, R., Ni, B., Gu, X., Zhang, X., Zuo, P., et al. (2017). Inferring electromagnetic ion cyclotron wave intensity from low altitude POES proton flux measurements: A detailed case study with conjugate Van Allen Probes observations. *Advances in Space Research*, 59(6), 1568–1576. <https://doi.org/10.1016/j.asr.2016.12.035>

Zhao, Y., Zhu, H., & Chen, H. (2023). Expected emic wave generation and unexpected ms wave disruption in a magnetic dip. *Journal of Geophysical Research: Space Physics*, 128(8), e2023JA031776. <https://doi.org/10.1029/2023JA031776>

Zhu, H., Chen, L., Artemyev, A. V., Zhang, X.-J., & Breneman, A. W. (2021). Superposed epoch analyses of electron-driven and proton-driven magnetic dips. *Geophysical Research Letters*, 48(21), e94934. <https://doi.org/10.1029/2021GL094934>